Novel approach of laser formation and characterization of multi-faceted bi-lateral/front continuous PSi layer

Rasha B. Rashid[1] · Alwan M. Alwan[2] · Amer B. Dheyab[3]

Abstract

In this novel research, three laser beams of equal intensities were employed to form multiple orthogonal Porous Silicon (PSi) layers on the bilateral and the front silicon substrate. The morphology of the synthesized PSi layers, composed of multi-axis of Si nanocrystallites columns, pores and mud-like structures, and perpendicular to each other. These specific Psi morphologies are created via two various laser-supporting etching pathways with an appropriate optical system consisting of different types of lenses, three laser diodes of similar power 100 mW with a short wavelength of 410 nm were employed as a photonic source during the etching process. The morphological, structural, and optical properties of the bi-lateral and top PSi layers were investigated extensively. The obtained results display the existence of ultra-high density of Si columns, pores and trenches in the front and the opposite lateral PSi layer. The grain sizes, surface morphology, PL emission and chemical bonds of the bi-lateral porous layers show a high degree of symmetry. This unique PSi layer can be suggested as an excellent choice for improving the surface area and decreasing the surface leakage current in porous silicon-based gas sensor devices.

Keywords PSi layer · Gas sensors · Laser beam · Nano-crystallite

1 Introduction

Porous silicon (PSi) is defined as a tangled network of different silicon nanostructures, which are surrounded by pores of different dimensions and shapes [1]. PSi is characterized by a set of unique properties; it has a very high surface area and a very high electrical resistivity compared to the resistivity of an intrinsic silicon substrate. The resistivity increases as a function of the porosity of the layer [2]. The adsorption rate of chemicals on the porous structure increases with the surface area and the density of nanocrystallites within the porous layer [3]. Therefore, PSi is considered one of the important materials that are utilised in different applications, such as plasmonic sensors of various types, photonic sensors, and gas sensors [4–6]. PSi is usually synthesized by photochemical etching, which is mostly done in the presence of light or a laser beam with an external electric current or in the absence of an electric current [7, 8]. The presence of light or a laser beam is considered essential to provide the necessary charge carriers to complete the dissolution process of silicon within the hydrofluoric acid solution, especially if the crystalline silicon sample used is of the donor type [9].

The effectiveness of any PSi layer towards any type of application, particularly in the field of electrically detecting toxic gases and organic vapors, is dependent upon several important parameters, including the layer's surface area, the surface density of the nanostructures contained therein, as well as the layer's morphology [10]. Therefore, elevating these important parameters would improve the performance of sensors manufactured from a PSi layer. In addition, reducing the surface leakage current in any PSi gas sensor is considered one of the very important factors in reducing the error rate in electrical measurements, in addition to reducing the silicon detection limit of the sensor [11]. Thus, using a multi-faceted continuous PSi layer (front and bi-lateral) is considered one of the important scientific concepts to improve the performance of sensors, because it provides an increase in the total surface area of the sensor while reducing the surface leakage current to the lowest possible extent [12].

✉ Alwan M. Alwan
   alkrzsm@yahoo.com

1   General Directorate Vocational Education, Ministry of Education, Baghdad, Iraq

2   School of Applied Science, University of Technology, Baghdad, Iraq

3   Directorate of Material Research, Ministry of Science and Technology, Baghdad, Iraq

Consequently, based on what was previously mentioned, the novelty of this research is to prepare and study the overall characteristics of a frontal and bi-lateral multifaceted continuous PSi layer for the purpose of increasing the surface area of the sensor while reducing the surface leakage current. The potential application of a multifaceted continuous Psi layer with double laser beams has a high degree of novelty.

2 Experimental procedure

In this research, distinct multiple orthogonal PSi layers of multi-faceted bi-lateral/front continuous layer were created. These layers had the morphology of synthesized PSi layers and were composed of multi-axis Si nanocrystallite columns, pores and muds-like structures, perpendicular to each other across the top thickness of the substrate. This distinct multiple orthogonal PSi layer was generated for the first time using two different etching methods conducted simultaneously, using three laser beams at similar wavelengths and intensity. The first etching method for the creation of the bi-lateral porous layers was the photochemical etching process using two laser beams with a wavelength of 410 nm and an optical power of 100 mW. The bi-lateral etching method, (photochemical) etching was conducted without the use of an external etching current and the duration of the laser beam was 20 min. The lateral laser beams were focused in the form of a straight line instead of a circular spot, and this was done using two cylindrical lenses one for each silicon-sided with a focal length of 15 cm. The second etching method was conducted for the front layer. A supportive laser etching with a 100 mW laser power, 410 nm wavelength and an etching current of 30 mA for a period of time of 20 min was utilized. The front laser beam was focused in the form of a circular irradiation area of about 1.5 cm^2, on the front face of the crystalline Si surface using a biconvex lens with a 20 cm focal length. This multiple etching method on different silicon surfaces was used for the first time (novel approach). This etching technique achieves the generation of a porous layer that provides multi-axis Si nanocrystallites, ensuring high adsorption of gas molecules to be detected very efficiently. The side etching process was done without using a platinum electrode, so it is a chemical etching supported by a laser beam. The electrical current used in etching the upper surface of the silicon surface is an external current applied by a power supply with a laser beam (laser-assisted electrochemical etching). The advantage of this double etching is to obtain three-dimensional nanostructures and to obtain a distinct surface area, which is difficult to obtain with conventional single etching methods. This multiple orthogonal surface etching method for

the creation of front and bi-lateral porous layers' structures is shown in Fig. 1.

The etching process was carried out on an n-type crystalline Si substrate of 100 orientation and 10 Ω·cm resistivity in 20% HF concentration, (1:1) electrolyte solution (HF 40%: C_2H_5OH 99.99%).

In the creation of the front PSi layer (second etching method) which is supportive with laser, the Si substrate acted as an anode and a platinum ring as a cathode. The experiment was carried out at room temperature. The porosity and layer thickness of the created PSi were calculated gravimetrically and from the x-section image of FE-SEM. The morphological properties of formed structures were investigated by ZEISS Field Emission scanning electron microscopy (FE-SEM), while the photoluminescence PL spectrum was conducted using Jobin–Yvon T64000 with CW 320 nm, 350 mW He–Cd laser.

The structural properties of the front and each of the lateral silicon faces were studied by analyzing the FTIR and X-ray diffraction (XRD) patterns.

3 Results and discussion

3.1 Characterization of front and bi-lateral PSi layers

The morphologies aspects (pores, muds, and columns) of the synthesized layer were investigated extensively, based on the surface and x-section FE-SEM image of the front PSi layer, while the porosity and layer thickness of front and bilateral (right- and left-sided) porous silicon layers were studied gravimetrically [13]. The value of layer thickness of right- and left-sided were about 1.8 and 1.87 μm, respectively, while the front layer was about 2.3 μm. The porosity of the front, right- and left-sided layers were around 68%, 67.5% and 74%, respectively. Pores can also be formed through perforation, where external forces or objects puncture the front layer, creating holes or gaps. This can happen through mechanical impact, etching, or other penetrating actions. Based on the Bruggeman effective medium approximation theory, which involves considering the porous silicon layer as a complex network of pores surrounded by silicon nanostructures [14], the dielectric constant $\varepsilon_{r_{Psi}}$ of the right, left and front layers were about 4.1, 4.4 and 3.8, respectively [15–20]. $\varepsilon_{r_{Psi}}$ is related to the porosity of the layer by the following formula [16]:

$$\varepsilon_{r_{Psi}} = \varepsilon_{r_{Si}} - p\left(\varepsilon_{r_{Si}} - \varepsilon_{r_{pore}}\right) \tag{1}$$

where $\varepsilon_{r_{pore}}$ and $\varepsilon_{r_{Si}}$ are the dielectric constant of air which fills the pores and Si, respectively. As the porosity increases,
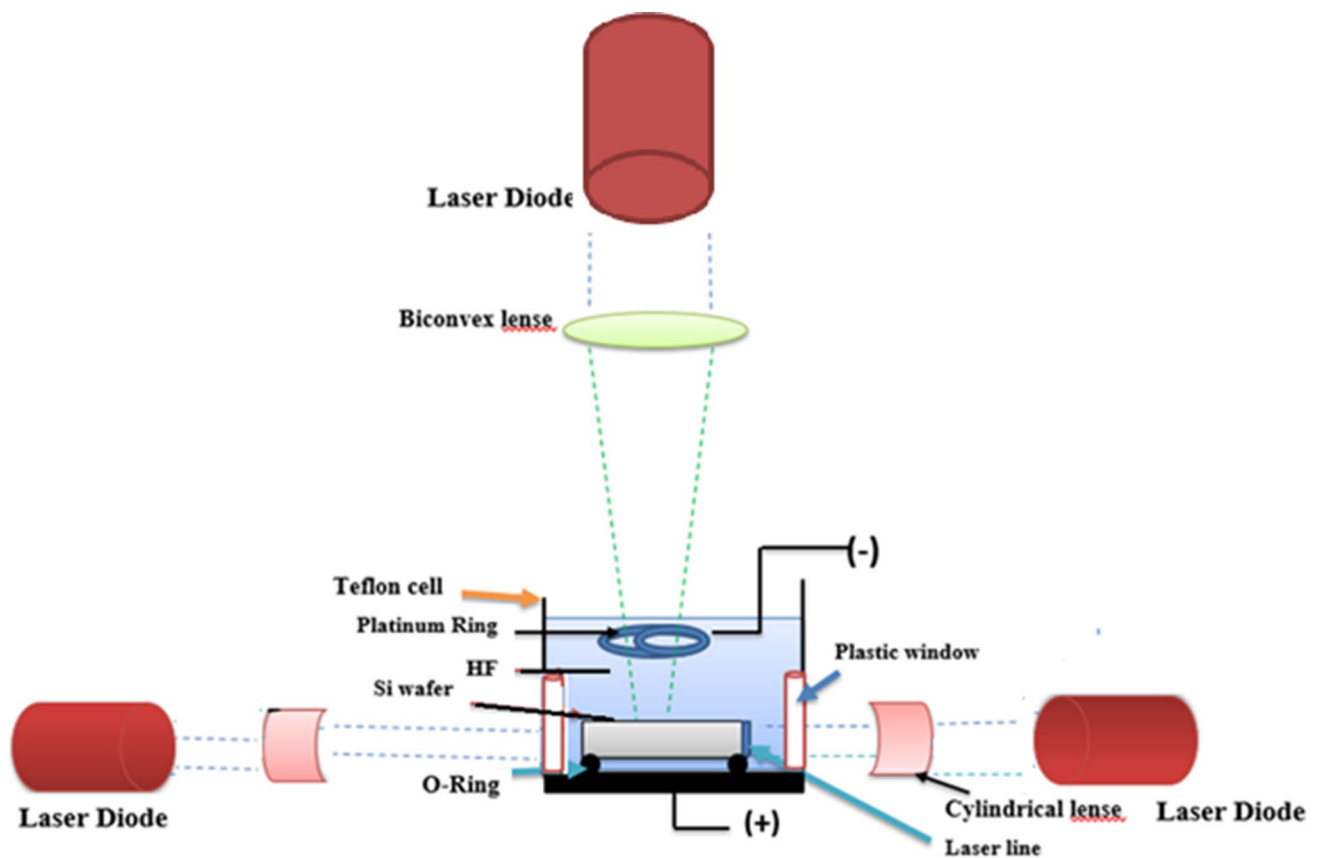
Fig. 1 Experimental setup for creating multiple orthogonal PSi layers

the $\varepsilon_{r_{Psi}}$ will decrease due to the increase in the number of void spaces within the porous matrix.

The morphological characteristics of the front porous silicon surface indicate the presence of a complex network of vertical silicon columns having different dimensions arranged perpendicularly to the silicon surface, in addition to the presence of distinct pores irregularly distributed on the silicon surface, as it is clear in Fig. 2a. Whereas the surface morphology of the bilateral (right and left side) porous silicon layers, Fig. 2b, c, clearly indicate that the surface of the porous silicon contains a distinctive formation of mud-like silicon texture of various dimensions with almost rectangular shapes distributed in an unorganized manner on the surface, these muds were separated by vertical trenches with varied width. Each individual silicon mud consisted of ultrafine pores separated by silicon columns distributed perpendicular to the surface. The dimension variance of the silicon muds and trenches was attributed to the Gaussian distribution of the laser beam intensity along the sides of the Si substrate.

In the front PSi layer, the surface density of pores was about (3×10^6 pores/cm^2) which was lower than that of the surface density of columns (8×10^9 columns/cm^2). Whereas for the right and the left layers, the densities of the mud were

about (7×10^7 and 5×10^7) muds/cm^2, respectively. This little variation in the density of mud on both sides of the lateral porous layer (right and left) was mainly caused by the symmetry of the etching method on both sides, which occurred at a constant laser intensity and an identical etching time. However, the difference in the surface density of silicon columns and the silicon muds between the front porous layer and bilateral PSi layers was due to the difference in the etching method utilized [21]. Despite the equal intensity of the laser beam in the two etching methods, the presence of the external electric current in etching the front layer enhances the dissolution of the silicon and thus increases the rate of the etching in all directions. Thus, an increase in the surface density of the resulting nanostructures (columns) took place [22].

Figure 3a–d illustrates the histogram of the size distribution of columns and pores in the front layer and mud area of the right layer and the left layer. The columns and pores sizes are shown in Fig. 3a, b, the sizes of the pores were in the range of 300–900 nm, while the apex sizes of columns ranged from 25 to 150 nm. The peaks of the histogram of pores and columns are around 900 and 45 nm, respectively. The mud area of the right and the left bilateral porous layer, shown in Fig. 3c, d, ranged from 0.1 to 0.4 μm^2 and the peak

Fig. 2 Illustrates the surface morphology of porous silicon **a** front layer, **b** right layer and **c** left layer
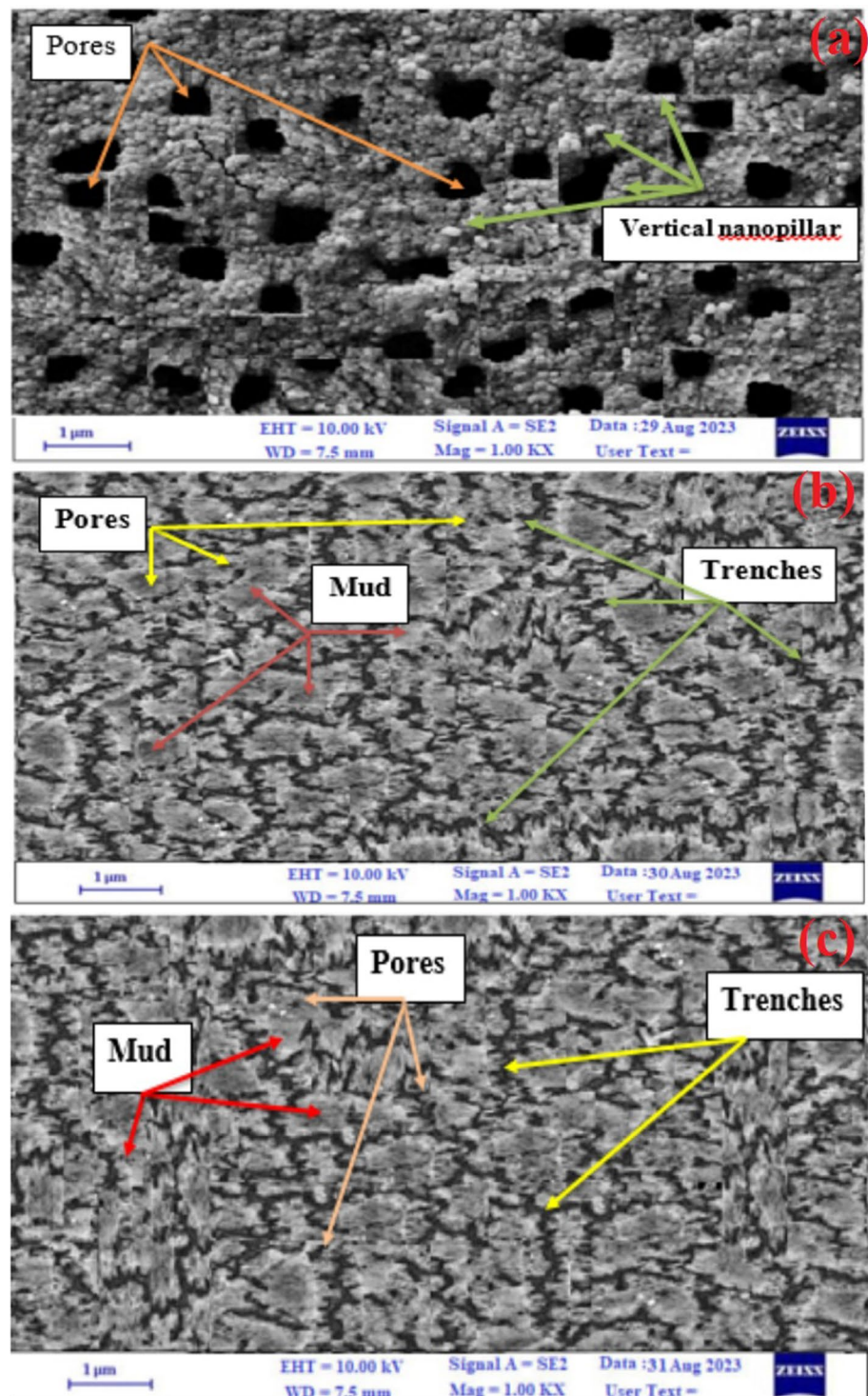

of the histogram of mud area of the right layer and the left layer were around 0.15 and 0.25 μm², respectively. The main reason for the difference in the area of the silicon muds for the left side and the right side is due to slight changes in the reflectivity of the side faces of the silicon, which in turn will lead to a slight difference in the intensity of the laser beam absorbed by the right side and the left side. The difference in

the intensity of the absorbed laser beam will lead to a change in the etching rate on each side, which in turn will lead to a change in the area of the silicone muds.

Figure 4b, c represents the x-section FE-SEM image of the right layer and the left bilateral porous layer. The PSi morphologies within the lateral porous layers consisted of double Si columns perpendicular to each other, while, the

Fig. 3 Histogram of size distribution **a** columns in the front layer, **b** pores in the front layer, **c** mud area of the right layer and **d** mud area of the left layer
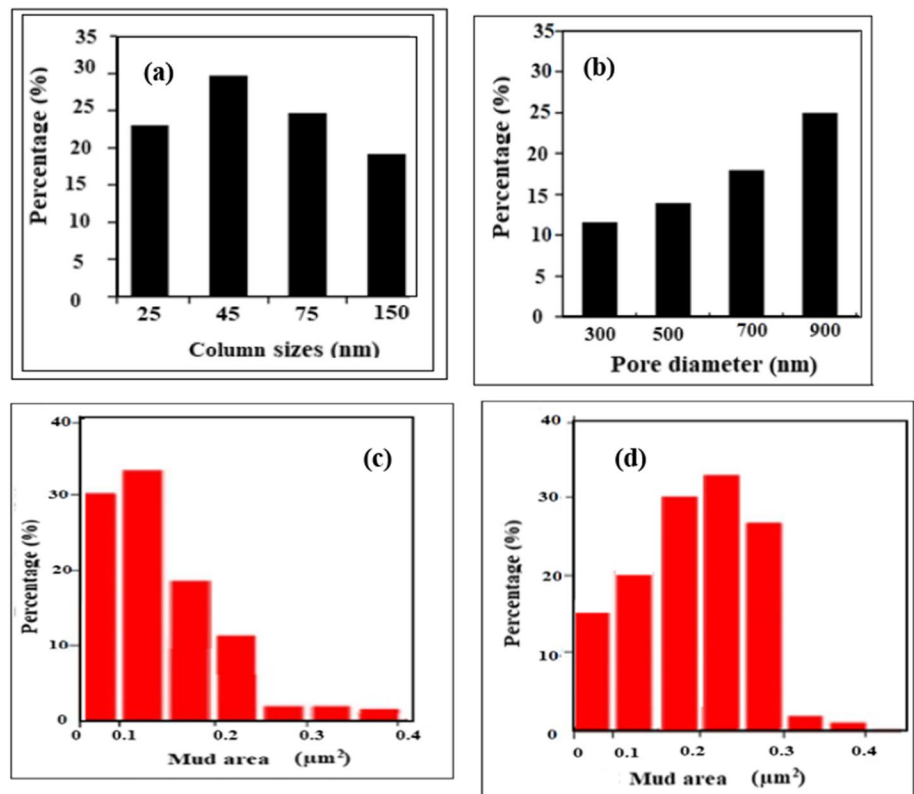
pores shown in the front layer were arranged vertically and uniformly along the Si surface.

The effects of laser intensity on the etching pathway and morphology can play a significant role in determining the resulting surface structures and properties. This process will modify the Si dissolution route during the PSi creation which leads to the existence of a complex network of nanostructures in the forms of pores, muds or columns. The formation mechanism behind these results can be understood based on the K. Cheah model [23–26], the etching pathway in a process that depends on the rate of photo-generated electron–hole couples can indeed be influenced by the intensity of the laser used. When the laser intensity increases, it can lead to a higher rate of photo-generated electron–hole pairs.

In supportive laser etching with external current, the current plays a significant role in providing the required positive holes for activating the silicon dissolution process [27]. The number of charge carriers (N) which was generated as a result of applying an external current is given via the following formula [16]:

$$N = \frac{t m_{Si} J}{q p_{Si} V_d} \tag{2}$$

where m_{si} is the mass of a Si atom, J is the current density, q is the elementary charge, P_{si} is the density of Si, V_d is the dissolved volume of silicon and t is the etching interval.

Whereas in the case of a photochemical etching process, only the photo-generated e–h + couples take place. under the condition of a uniform generation rate of h + within the space charge district, the rate of charge generation is expressed by the following formula [28]:

$$G = \frac{\varnothing_a}{T} \tag{3}$$

Meanwhile

$$\varnothing_a = \varnothing_o \left(1 - r_{PS}\right)\left(1 - e^{-\alpha T}\right) \tag{4}$$

where is $\varnothing_a$ the amount of absorbed light in a space charge district of thickness T, $\varnothing_o$ is the incident photon flux, α is the absorption coefficient and r_{PS} is the reflectivity of PS which is expressed by the following formula [18]:

$$r_{PS} = \left(n_{PS} - 1 | n_{PS} + 1\right)^2 \tag{5}$$

where n_{PS} is the reflective index of the porous layer and is given by the following formula [28]:

$$n_{PS} = \sqrt{\varepsilon_{r_{Psi}}} \tag{6}$$

The FTIR spectrum provides very accurate information about the chemical bonds present on the surfaces of both the front porous silicon layer and the bilateral porous silicon layers. Figure 5a–c presents the FTIR spectra of porous

Fig. 4 x-section FE-SEM images of the bilateral porous layer. **a** Right and **b** left
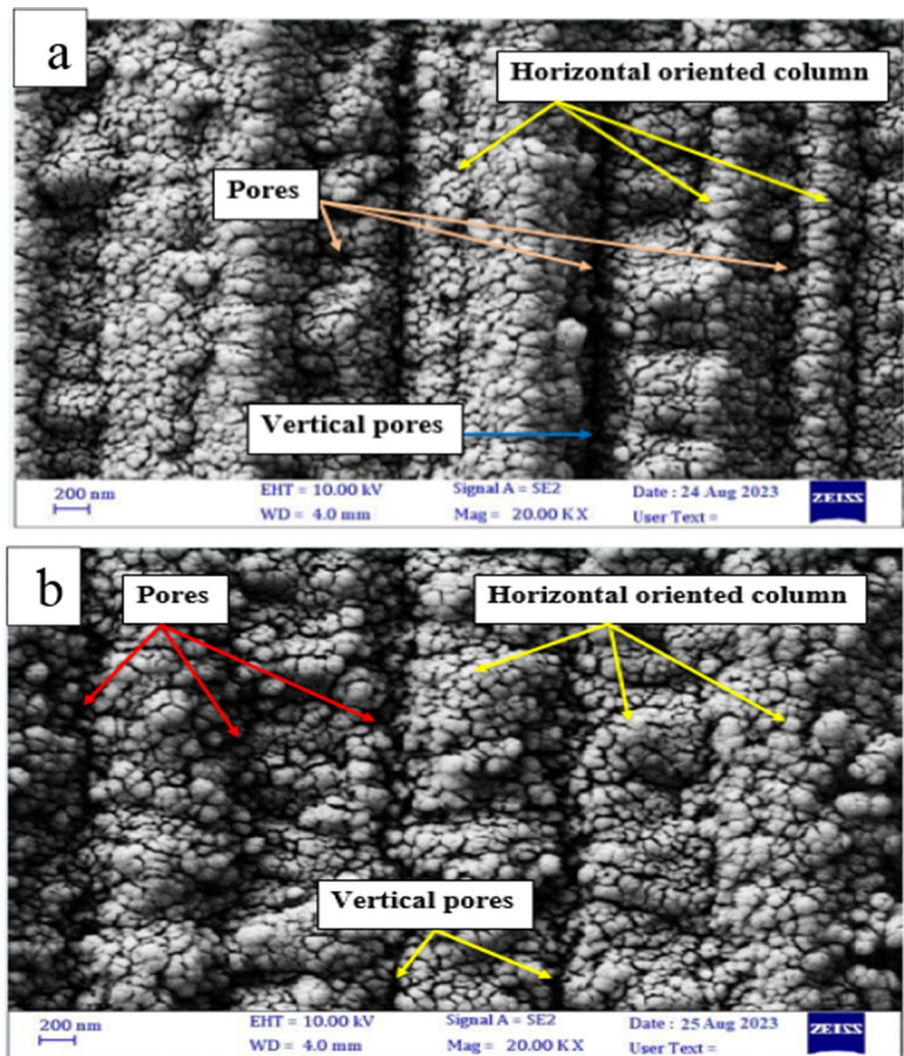
silicon surfaces within the wavenumber range (600–1500 cm^{-1}). Based on the resulting spectrum, the porous silicon surfaces contain vibrational bonds of different wavenumbers and intensities, which are naturally attributed to the front and lateral surfaces of the porous silicon. The intensity of these vibrations varies according to the etching method. The intensity of the bond vibrations of the front porous silicon layer (Fig. 5a), is higher than its counterparts in the bilateral porous silicon (right and left) layers (Fig. 5b, c), which are correspondent to each other. These molecular vibrations indicate the following bonds: bending vibration of mono hydride SiH, tri hydride SiH3 and the di-hydrides SiH2 within the wavenumber range from 600 to 1119 cm^{-1} [29–33]. The peak intensity of these hydrogenated bonds is usually located on the surfaces and the inner sides of the silicon columns and pores.

The laser-supporting etching pathway for the front porous silicon layer provides higher efficiency than the photochemical etching pathway used in the side porous silicon layers. Therefore, the dissolution of the silicon atoms in the front porous silicon layer is more efficient. Thus, the density of the resulting types of hydrogen bonds is more intense.

The XRD patterns of the front porous layer and bilateral PSi layers are shown in Fig. 6a–c, respectively. The X-ray diffraction patterns generated from the front and bilateral layers were characterized by the presence of distinct XRD peaks and are consistent with the XRD data regarding diffraction values, (JCPDS). The XRD peaks of both types of porous silicon layers are characterized by the presence of only one peak indicating that the porous silicon is (100) plane monocrystalline at a diffraction angle (2θ) of about 30°, with a clear difference in full width half maximum (FWHM) (β). These differences in FWHM produced by the front and the bilateral porous silicon layers is attributed to the difference in the etching process, which lead to the emergence of slight differences in the dimensions of the three directional porous silicon layers. The smaller
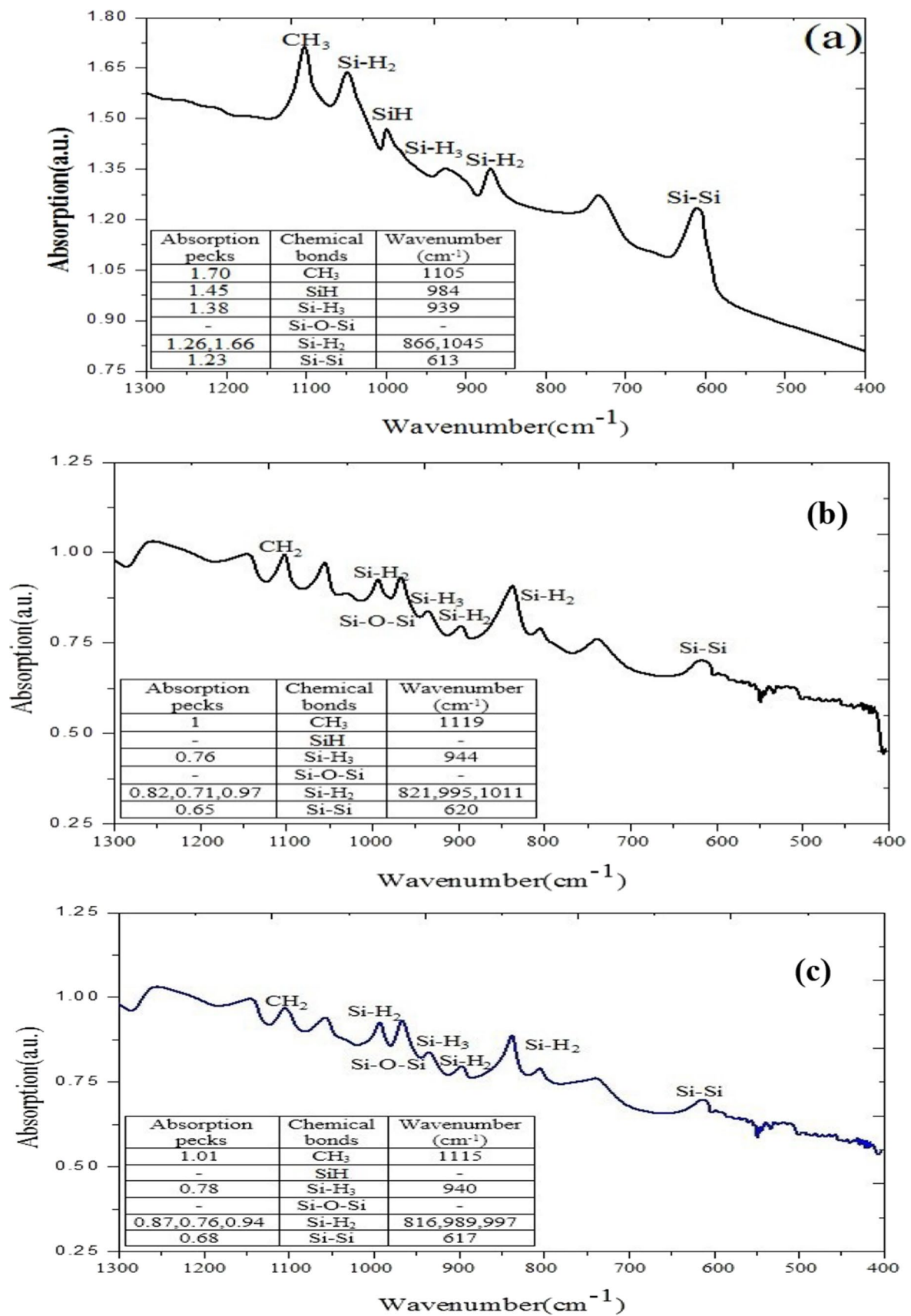
Fig. 5 FTIR spectra of PSi **a** front layer, **b** right layer and **c** left layer
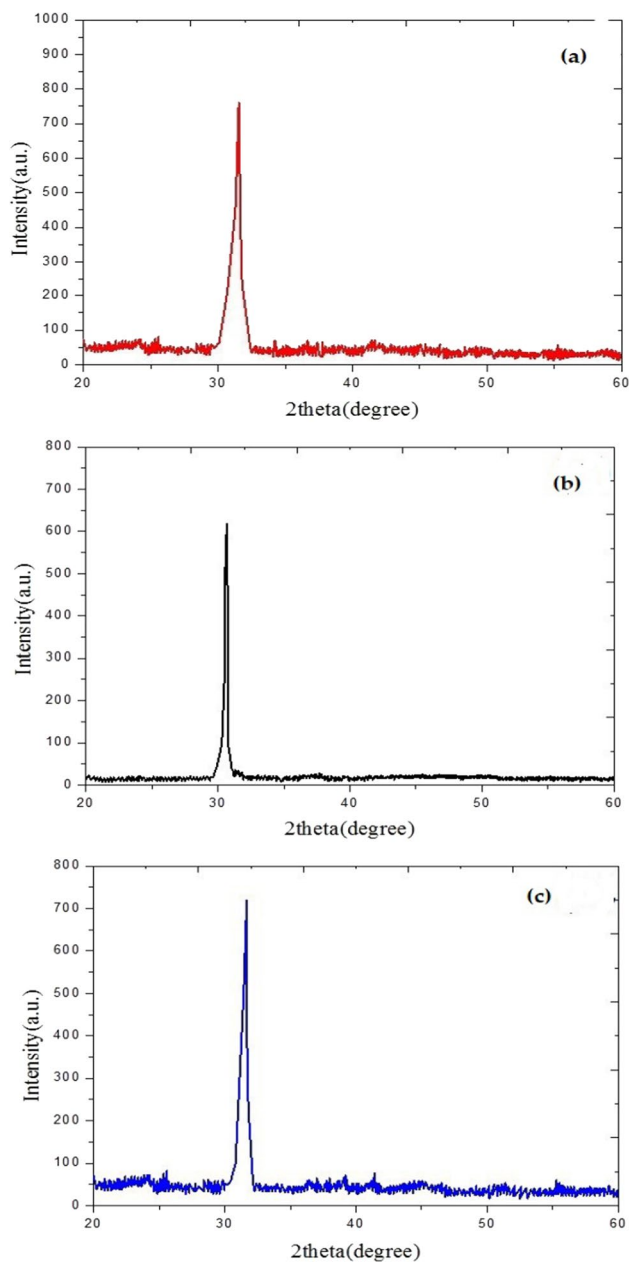
Fig. 6 XRD patterns of Psi **a** front layer, **b** right layer and **c** left layer

the dimensions of the silicon crystals, the FWHM will obviously increase [34].

The sizes of the silicon nanocrystals within the front porous silicon layer and the bilateral porous silicon layers (*d*) were calculated based on Scherrer equation [33, 35]:

$$L = F\lambda / \beta \cos\theta \qquad (7)$$

where *L* represents the sizes of the crystals in the porous silicon layer, *F* is a dimensionless shape factor, with a value close to unity, *λ* is the X-ray wavelength, *β* is the line

broadening at half the maximum intensity (FWHM), *θ* is the Bragg angle. The photoluminescence spectra (PL) of the front porous layer and bilateral PSi layers is shown in Fig. 7. The emission wavelength and intensity are governed by the morphology of the porous layer, the density and the dimensions of the Si nanocrystallites. The emission wavelength, intensity, dimension of nanocrystallites and energy gap (E_g) of porous silicon layer are presented in Table 1. As shown in the table, shortest emission wavelength, i.e., higher porous silicon energy gap, was reached by the front porous layer, while, longest emission wavelength, i.e., lower porous silicon energy gap, was documented with the bilateral PSi layers. In addition, the lowest FWHM emission of PL wavelength with blue shift and much higher PL intensity was realized with front porous layer compared with the bilateral PSi layers. This is mainly related to the presence of the external electric current in etching the front layer, this current will enhance the dissolution of the silicon and thus increases the silicon etching rate. While, for the bilateral PSi (right and left) layers, there is a little variation in emission wavelength, intensity, dimension of nanocrystallites and energy gap density in both lateral porous layers (right and left). This is mainly caused by the symmetry of the etching method on both sides, which occurs at a constant laser intensity and an identical etching time. The PL intensity is chiefly
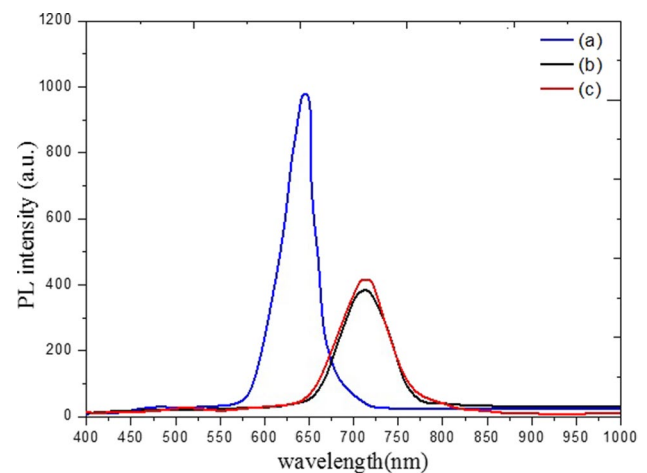

Fig. 7 PL spectra of PSi **a** front layer, **b** right layer and **c** left layer

Table 1 PL emission wavelength, intensity, dimension of nanocrystallites and energy gap of porous silicon layer

Porous type	Emission wavelength (nm)	Intensity (a.u.)	Nanocrystallites *L* (nm)	E_g (eV)
Front PSi	650	956	3.16	1.9
Bilateral left	725	380	3.87	1.71
Bilateral right	730	350	3.92	1.7

influenced by the quantity of nanocrystallites' luminescence in the porous layer due to the increase of e–h + recombination rate [32]. The dependence of energy gap of porous silicon on their sizes was in excellent agreement with the proposed model by Alwan et al. as revealed in the following formula [33]:

$$\mathbf{Eg} = (\mathbf{Si}) + \frac{\left(\mathbf{h}^2\boldsymbol{\pi}^2\mathbf{D}\right)}{\left(2\mathbf{mr}*\mathbf{L}^2\right)} \qquad (8)$$

where $mr*$ is the reduced effective mass, D is a constant equals 2 for a quantum pillar and 3 for SiQDs, while L is the confinement dimension.

This slight change in the properties of the bilateral layers of porous silicon is mainly due to the change in the roughness of the left and right sides of the substrate resulting from cutting the silicon. As the roughness of the cutting area increases, the reflectivity of the silicon surface decreases, and thus the rate of photon absorption increases, which in turn will change the etching rate.

4 Conclusion

In this research, three laser beams of equal intensities were employed to form three directions PSi continuous layers. These specific PSi morphologies were created simultaneously via laser supporting and photochemical etching pathways. The morphology of this multi-faceted bi-lateral/front continuous PSi layer is composed of a multi-axis of Si nanocrystallite columns, pores and mud-like structures, perpendicular to each other. The morphological, structural, and optical properties of the bilateral and top PSi, show strong dependence on the etching pathway. An ultra-high density of Si columns, pores and trenches was recognized in the front and bi-lateral PSi layer. The grain sizes, surface morphologies, PL emission and chemical bonds of the bi-lateral porous layers show a high degree of symmetry compared with the front porous layer. This unique multi-faceted bi-lateral/front continuous PSi morphology can be suggested as an excellent choice for improving the surface area and decreasing the surface leakage current in porous silicon-based gas sensor devices.

Author contributions We, the authors, all participated in the implementation of the experiments, the management of the data, and the preparation of the report for this research.

Data availability The data sets generated during and/or analyzed during the current study are available from the corresponding author upon reasonable request.

Declarations

Conflict of interest There are no conflicts of interest regarding the publication of this manuscript.

References

1. Z.H. Xiong, S. Yuan, Z.M. Jiang, J. Qin, C.W. Peil, S. Liao, X.M. Ding, X.Y. Hou, W. Xun, Photoluminescence studies of porous silicon microcavities. J. Lumin. **80**, 137–140 (1998)
2. L.T. Canham, Silicon quantum wire array fabrication by electrochemical and chemical dissolution of wafers. Appl. Phys. Lett. **57**, 1046–1104 (1990)
3. A. Stephen, K. Hashmi, G.J. Hutchings, Gold catalysis. Angew. Chem. Int. Ed. **45**, 7896–7936 (2006)
4. Y. Abdi, J. Derakhshandeh, P. Hashemi, S. Mohajerzadeh, F. Karbassian et al., Light-emitting nano-porous silicon structures fabricated using a plasma hydrogenation technique. Mater. Sci. Eng. B **124–125**, 483–487 (2005)
5. M.A. Alwan, F.J. Muslim, A.C. Aseel, Controllable synthetization of Au nanoparticles by laser enhanced wet KOH etching process. J. Phys. Conf. Ser. **1963**, 012009 (2021)
6. X. Guo, S. Xu, L. Zhao, W. Lu, F. Zhang, D.G. Evans et al., One-step hydrothermal crystallization of a layered double hydroxide/alumina bilayer film on aluminum and its corrosion resist lance properties. Langmuir **25**(17), 9894–9897 (2009)
7. J. Wang, D. Li, Q. Liu, X. Yin, Y. Zhang, X. Jing et al., Fabrication of hydrophobic surface with hierarchical structure on Mg alloy and its corrosion resistance. Electrochim. Acta **55**(22), 6897–6906 (2010)
8. A.M. Alwan, R.B. Rashid, A.B. Dheyab, Morphological and electrical properties of gold nanoparticles/macroporous silicon for CO_2. Iraqi J. Sci. (IJS) **59**(1A), 57–66 (2018)
9. J. Ou, W. Hu, M. Xue, F. Wang, W. Li, Super hydrophobic surfaces on light alloy substrates fabricated by a versatile process and their corrosion protection. ACS Appl. Mater. Interfaces **5**(8), 3101–3107 (2013)
10. A.M. Alwan, D.A. Hashim, M.F. Jawad, Optimizing of porous silicon alloying process with bimetallic nanoparticles. Gold Bull. **51**, 175–184 (2018)
11. A.M. Alwan, Calculation of energy band gap of porous silicon based on the carrier transport mechanisms. Eng. Technol. **25**, 1143–1148 (2007)
12. Y. Fan, Z. Chen, J. Liang, Y. Wang, H. Chen, Preparation of superhydrophobic films on copper substrate for corrosion protection. Surf. Coat. Technol. **244**, 1–8 (2014)
13. Z. Wang, J. Gong, J. Ma, J. Xu, In situ growth of hierarchical bochmite on 2024 aluminum alloy surface as superhydrophobic materials. RSC Adv. **4**(28), 143–214 (2014)
14. A.S. Ruqaya, S.M. Mohammed, illumination effects on the physical properties of porous silicon prepared by PECE. Appl. Nanosci. **5**, 1279–1283 (2018)
15. L.A. Wali, K.K. Hasan, A.M. Alwan, An investigation of efficient detection of ultra-low concentration of penicillins in milk using AuNPs/PSi hybrid structure. Plasmonics **15**(4), 985–993 (2020)
16. A.M. Alwan, I.A. Naseef, A.B. Dheyab, Well controlling of plasmonic features of gold nanoparticles on macro porous silicon substrate by HF acid concentration. Plasmonics **13**(6), 2037–2045 (2018)
17. S.H. Xu, Z.H. Xiong, L.L. Gu, Y. Liu, X.M. Ding, J. Zi, X.Y. Hou, Preparation of one-dimensional porous silicon photonic quantum-well structures. Appl. Phys. A **76**, 589–592 (2003)

18. M.S. Detlef, Scherrer grain-size analysis adapted to grazingincidence scattering with area detectors. J. Appl. Cryst **42**, 1030–1034 (2009)

19. A.H. Duaa, M.A. Alwan, F.J. Muslim, An investigation of structural properties of monometallic (Ag, Pd) and bimetallic (Ag@Pd) nanoparticles growth on macro porous silicon. Int. J. Nanoelectr. Mater. **11**, 461–472 (2018)

20. A.M. Alwan, A.A. Jabbar, Design and fabrication of nanostructures silicon photodiode. Mod. Appl. Sci. **5**(1), 106 (2011)

21. C. Zhai, Y. Li, Y. Peng, T. Xu, Detection of chlorpyrifos in apples using gold nanoparticles based on surface enhanced Raman spectroscopy. Int. J. Agric. Biol. Eng. **8**, 113–120 (2015)

22. Y. Liu, Y. Zhang, H. Wang, B. Ye, Detection of pesticides on navel orange skin by surface-enhanced Raman spectroscopy coupled with Ag nanostructures. Int. J. Agric. Biol. Eng. **9**(2), 179–185 (2016)

23. A. Virga, P. Rivolo, E. Descrovi, A. Chiolerio, G. Digregorio, F. Frascella, SERS active Ag nanoparticles in mesoporous silicon: detection of organic molecules and peptide–antibody assays. J. Raman Spectrosc. **43**, 730–736 (2012)

24. R.B. Rashid, A.B. Dheyab, A.M. Alwan, Enhancing the performance of p_n junction Si solar cells by integrating silver core and gold shell nano-particles. Opt. Quant. Electron. (2022). https://doi.org/10.1007/s11082-021-03464-z

25. S. Devarajan, B. Vimalan, S. Sampath, Phase transfer of Au–Ag alloy nanoparticles from aqueousmedium to an organic solvent: effect of aging of surfactant on the formation of Ag-rich alloy compositions. J. Colloid Interface Sci. **278**, 126–132 (2004)

26. A.A. Khalaf, A.H. Attallah, A.B. Dheyab, A.M. Alwan, Influence of magnetic field on the characteristics of n-type PSi prepared by photo-electro-chemical etching process. J. Phys. Conf. Ser. **1963**, 012–015 (2021)

27. A.E. Chalhoub, N. Semmar, L. Coudron, G. Gautier, C. Boulmer-Leborgne et al., Thermal conductivity measurement of porous silicon by the pulsed-photothermal method. J. Phys. D Appl. Phys. **44**, 1–16 (2011)

28. M.A. Alwan, A.B. Dheyab, A.J. Allaa, Study of the influence of incorporation of gold nanoparticles on the modified porous silicon sensor for petroleum gas detection. Eng. Technol. J. **8**, 811–815 (2017)

29. Z. Irena, R. Krzysztof, K. Małgorzata, The effect of isopropyl alcohol concentration on the etching process of Si-substrates in KOH solutions. Sens. Actuators A **171**, 436–445 (2011)

30. M.A. Gosalvez, Y. Xing, K. Sato, Analytical solution of the continuous cellular automaton for anisotropic etching. J. Microelectromech. Syst. **17**, 410–431 (2008)

31. L.A. Wali, A.B. Dheyab, A.M. Alwan, Study the influence of shell thickness in bimetallic Ag core and Au shell configurations integrated in bare Si PN junction solar cells. Mater. Sci. Eng. B Solid State Mater. Adv. Technol. **288**, 116210 (2023)

32. R.K. Soni, G.R. Bassam, S.C. Abbi, Laser-controlled photoluminescence characteristics of silicon nanocrystallites produced by laser-induced etching. Appl. Surf. Sci. **214**, 151–160 (2003)

33. A.M. Alwan, D.A. Hashim, M.F. Jawad, Efficient bimetallic nanoparticles embedded-porous silicon CO gas sensor. Solid State Electron. **153**, 37–45 (2019)

34. A.M. Alwan, O.A. Abdulrazaq, Aging effect on the photosynthesized porous silicon. Int. J. Mod. Phys. B **22**, 417–422 (2008)

35. H.R. Abed, A.M. Alwan, A.A. Yousif et al., Efficient SnO_2/CuO/porous silicon nanocomposites structure for NH_3 gas sensing by incorporating CuO nanoparticles. Opt. Quantum Electron. **51**(10), 333 (2019)